Applied Magnetic Resonance
https://doi.org/10.1007/s00723-022-01505-8

Applied
Magnetic Resonance

ORIGINAL PAPER

Coupling Sub-nanoliter BDPA Organic Radical Spin Ensembles with YBCO Inverse Anapole Resonators

Claudio Bonizzoni[1,2] · Maksut Maksutoglu[3] · Alberto Ghirri[2] · Johan van Tol[4] · Bulat Rameev[3] · Marco Affronte[1]

Received: 21 June 2022 / Revised: 9 September 2022 / Accepted: 30 September 2022

Abstract
We report the development and test of planar microwave Inverse Anapole Resonators (IARs) made of superconducting Yttrium Barium Copper Oxide (YBCO) for electron spin resonance spectroscopy on small samples. We first characterize our resonators in zero field and then by carrying out transmission spectroscopy on a diluted α,γ-bisdiphenylene-β-phenylally (BDPA) organic radical spin ensemble in an applied magnetic field. These IARs allow us to carry out electron spin resonance spectroscopy both in continuous-wave and pulsed-wave mode, and to estimate the spin memory time of BDPA. The comparison with the results obtained for the same sample on typical linear coplanar resonators shows an improvement by ≈ 2 - up to 3 – orders of magnitude in spin sensitivity, with effective sensing volumes below 1 nanoliter. The best sensitivity we achieved is $S \approx 10^7\,\mathrm{spin}/\sqrt{\mathrm{Hz}}$ in the pulsed-wave regime. These results compare well with similar experiments reported in the literature.

1 Introduction

Increasing the strength of the interaction with a microwave (MW) field is highly desirable when addressing electronic spins. The strategy typically followed in circuit Quantum ElectroDynamics (circuit QED) experiments is to use tightly confined modes (down to few μm—few tens of μm) of planar microwave resonator to enhance the single spin-photon coupling rate [1, 2]. An additional enhancement of the single spin coupling rate by a factor $\sqrt{N}$ (being N the number of spins involved) is obtained using spin ensembles [3, 4]. For instance, this strategy has been largely exploited to reach the coherent and the strong coupling regime between MW photons and several

M. Maksutoglu and A. Ghirri are contributed equally to this work.

✉ Claudio Bonizzoni
claudio.bonizzoni@unimore.it

Extended author information available on the last page of the article

Published online: 02 November 2022

spin ensembles, such as Nitrogen Vacancy (NV) centers [5–7], Erbium-doped inorganic crystals [8], Phosphorous [9] and Bismuth Donors in silicon [10] and molecular spins [11–16]. Conversely, small signals and reduced collective coupling rates are observed and only the weak coupling regime is expected when addressing small (i.e., low number of spins) ensembles. The parameter commonly used to quantify the detection capability of an experiment is the *spin sensitivity*, which is the minimum number of spins detectable in a measurement carried out at the detection limit (*signal-to-noise* ratio equal to one) for unitary bandwidth [17]. The lower the value of sensitivity the better the performance is. It is worth mentioning that this definition of sensitivity combines both intrinsic features of the device (*e.g.,* effect of the detection inductance of the geometry) as well as the characteristics of the output detection chain used after the device, such as specific features of amplification and/or acquisition electronics. This implies that enhancing spin sensitivity in electron spin resonance represents, overall, a technological challenge. It is also obvious that the definition of sensitivity above comes along with the definition of an effective equivalent detectable volume (or number of spins) which reduces as the sensitivity is improved.

Over the last decade, several ways to improve spin sensitivity have been proposed and successfully realized. A lot of effort was directed toward improving the geometry of the inductive parts of the resonators, which are responsible for the pick-up of the signal coming from the spins. This was done by focusing on closed-loop geometries rather than simpler linear coplanar ones, such as Ω-shaped resonators [18, 19], loop-gap resonators [20, 21] and oscillators with microcoils [22, 23]. Planar geometries in which the MW confinement is achieved in a very small micrometer-sized constriction of the device, such as ParPar resonators [24, 25] and Inverse Anapole Resonators [26], or coplanar resonators with micro-/nanoconstrictions [27] have been also developed. All these resonators were found to improve the spin sensitivity by several orders of magnitude with respect to conventional electron spin resonance (ESR) spectroscopy, reaching values which can be as good as $10^5 - 10^6\,\mathrm{spin}/\sqrt{\mathrm{Hz}}$ even at room temperature, corresponding to effective active volumes below a nanoliter (on the order of few tens—few hundreds of picoliters). The use of superconducting materials for the fabrication of resonators provides a natural way to increase the strength of the MW field as well as their sensitivity, but with the drawback of limiting their use at cryogenic temperatures and their applications (e.g., nonbiological) [24, 28]. For experiments involving superconducting resonators, improvements were made also in the choice of the materials and using high-kinetic inductance devices [29–32]. In these experiments the kinetic inductance of the superconducting material used for the resonator contributes, together with the geometrical one, to the detection. Finally, improvements were achieved also in the detection chain. Here in particular, the introduction of Josephson Parametric Amplifiers as a first (low temperature) amplification stage combined with the use of superconducting resonators with very narrow ($\approx$ μm) active elements, has further pushed the sensitivity to an unprecedented level, down to the quantum limit of detection [33]. State-of-the-art

sensitivities of $\approx 10^1$-10^3 spin/$\sqrt{\text{Hz}}$ and with volumes down to femtoliters have been recently reported [33–35].

In this work we investigate Inverse Anapole Resonators (hereafter, IARs) made of superconducting Yttrium Barium Copper Oxide ($YBa_2Cu_3O_7$, hereafter YBCO), a high-T_c superconductor, working at microwave frequency (7–15 GHz) to perform ESR spectroscopy over small spin ensembles. IAR geometries made of metallic conductors have been previously demonstrated to confine the MW magnetic field into a very small active volume on the order of 10–100 of picoliters [26]. Moreover, the analysis of the currents circulating inside these devices has shown that these geometries can efficiently suppress radiation losses, giving overall large quality factors, and well spatially separated magnetic and electric field maxima, reducing dielectric losses introduced by the sample [26]. The use of superconducting films is expected to enhance the MW field generated in the active region of the device and, hence, to improve the spin sensitivity. In addition, the device can take advantage of the high resilience of YBCO to externally applied static magnetic fields [14, 36]. However, to the best of our knowledge on the literature, superconducting IAR has never been investigated before. We test the transmission spectroscopy and the spin sensitivity achieved by our IAR both in continuous-wave (CW) and in pulsed-wave (PW) regime of excitation using a diluted ensemble of α,γ-bisdiphenylene-β-phenylally (BDPA) organic radical molecular spin, a standard commonly used for the calibration of spectrometers. To get more insights on IARs, we compare our results with microwave transmission spectroscopy performed on the same BDPA organic radical using two different linear coplanar resonators (hereafter, reference resonators) which we have extensively characterized and used in previous works. For the CW results, the reference resonator has a fundamental frequency $\nu_0 = 7.71$ GHz and a width for the central conductor of $w = 200\,\mu$m [14, 37]. For PW results, the reference resonator has fundamental frequency $\nu_0 = 6.91$ GHz and a width for the central conductor of $w = 600\,\mu$m [38]. An improvement of more than 2 (3 for some cases) orders of magnitudes is found in spin sensitivity with respect to our reference resonators, reaching $S = 8 \cdot 10^9$ spin/$\sqrt{\text{Hz}}$ for CW regime and up to $S \approx 10^7$ spin/$\sqrt{\text{Hz}}$ in PW regime, and with effective volumes in the sub-nanoliters ($\approx$ 0.1-0.2nL) range. Our results are found to be in line with the sensitivity values reported in the literature for the best IARs and also with the ones reported for similar planar microwave geometries.

2 Results

2.1 Inverse Anapole Resonators (IARs)

Inverse Anapole Resonators are shown in Fig. 1. The resonator has external dimensions of $4.4 \times 4.7\,\text{mm}^2$ and was designed to be fabricated with superconducting YBCO films (330 nm thickness) on Sapphire (430 µm thickness) substrate. It contains two D-shaped conducting parts (inner and outer radius

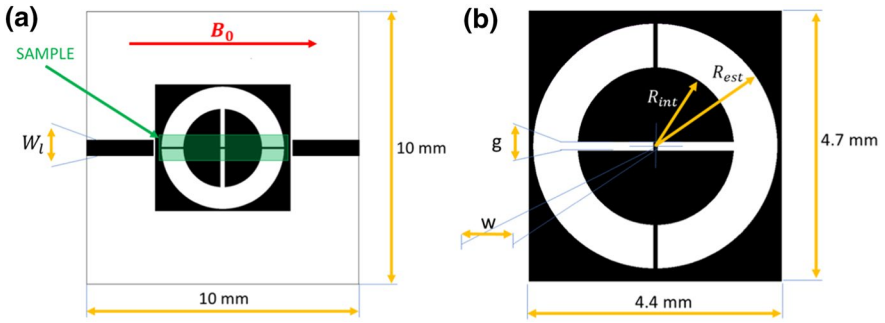

Fig. 1 **a** Sketch of the chip with the microstrip transmission line (width $W_l = 400\,\mu$m) with the Inverse Anapole Resonator (IAR) A1 on top. In the configuration used in this work the central conducting strip is aligned in order to be parallel to the axis of the microstrip transmission line. The chip carrying the IAR is not shown for better clarity. Green rectangle shows the position of the sample, while red arrow shows the direction of the static magnetic field, B_0. **b** Sketch of the anapole resonator used in our experiments with its dimensions ($W = 50\,\mu$m, $R_{\text{int}} = 1.35$mm, $R_{\text{ext}} = 2.15$mm $g = 178\,\mu$m). Black areas in figure correspond to YBCO. A photograph of the device in the configuration used in this work is shown in Supplementary Information (color figure online)

$R_{\text{int}} = 1.35$mm and $R_{\text{ext}} = 2.15$mm, respectively) connected by a narrow rectangular-shaped conducting strip with width $W = 50\,\mu$m. Hereafter, the resonator with these dimensions and geometry will be referred to as IAR A1. We additionally report in Supplementary Information the results obtained for a similar resonator (IAR A3) with the same size and dimensions but in which only the central conducting part has a different shape.

The chip carrying the resonator has no ground plane on the back and it is placed on top of a YBCO microstrip transmission line, which is used to probe the resonator with microwaves. The transmission line (width $W_l = 400\,\mu$m) has been fabricated on a separated chip with a back YBCO ground plane. The system consisting of IAR and feeding line has been mounted into a copper shielding box (see Sect. 5). In the configuration used in this work, IARs will be aligned on the transmission line in order to have the three conducting strips parallel to the longitudinal axis of the transmission line. Here we mention that IARs can have several additional working configurations, since their coupling with transmission line (and, consequently, their resonant frequency and transmission) can be tuned by changing the position and/or the angle of the resonator with respect to the line [24–26]. For the sake of completeness, we also mention that IARs, in principle, would allow one to work also in a configuration in which the static magnetic field is applied perpendicularly (out-of-plane direction) to the device. Although this dependence was not investigated in this work, our previous results obtained on the reference coplanar resonator [11] suggest that high-quality factors and resilient resonant peaks can also be obtained for out-of-plane orientations of the static magnetic field.

In Fig. 2 we report the transmission spectrum (scattering parameter S_{21}) of IAR A1 (see Sect. 5 for details). The transmission baseline is defined by the characteristics of the microstrip line used to feed the device. Several resonant modes are

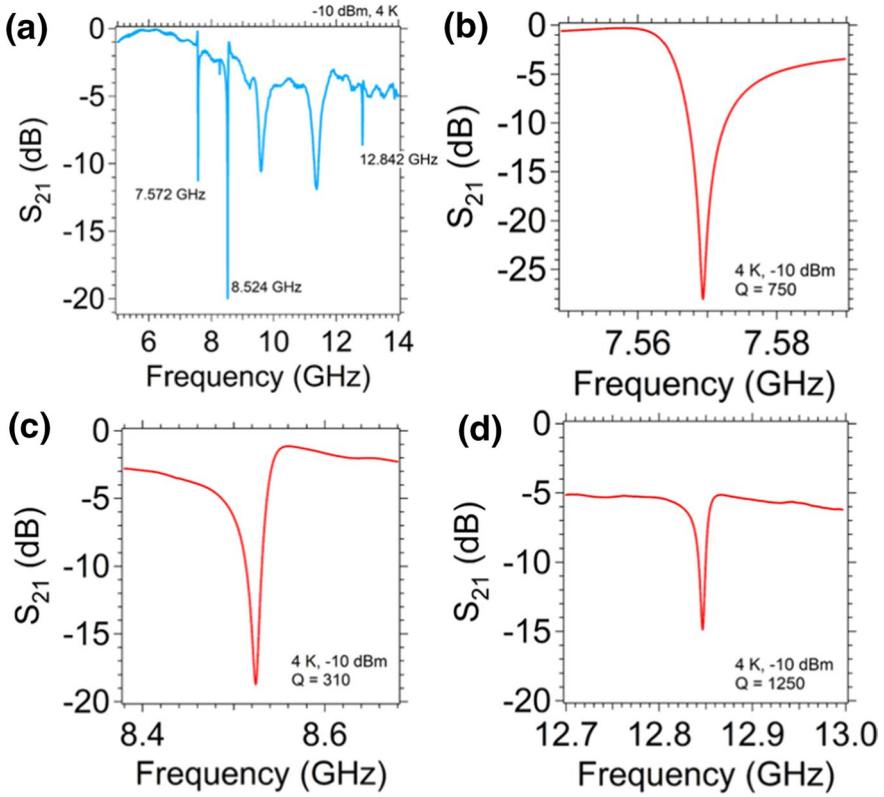

Fig. 2 **a** Full-range transmission spectra of IAR A1 taken in zero field at 4 K and with −10 dBm input power (blue line). **b–d** Zoom of the transmission of the three resonant modes investigated in this work

visible as dips in the transmission spectra, as a result of the excitation of the resonant modes in the coupling geometry used. In particular we can identify and fully attribute to IAR the three modes at $\approx 7.57, 8.52, 12.84$GHz (see Fig. 2, hereafter Mode #1, #2 and #3, respectively), which will be used in this work. Two additional dips are visible at $\approx 9.5, 11$GHz. Further inspection reveals that these resonances are given by the shielding box of the device and, hence, are not considered in this work. The quality factors of the three IAR modes are $Q = 750, 310$, and 1250, respectively. These modes are overcoupled to the transmission line, giving loaded quality factors.

2.2 Electromagnetic Simulation of IARs

In Fig. 3 we report the simulation of the MW magnetic field distributions for Modes #1, #2 and #3 of Fig. 2. For Mode #1 the oscillating field is mainly localized on the two outer conducting strips (the ones linking the D-shaped parts with the outer conductor), while there is no MW field in the central region. Conversely, for Mode #2 and #3 the MW distribution is localized over all the three conducting strips and the maximum

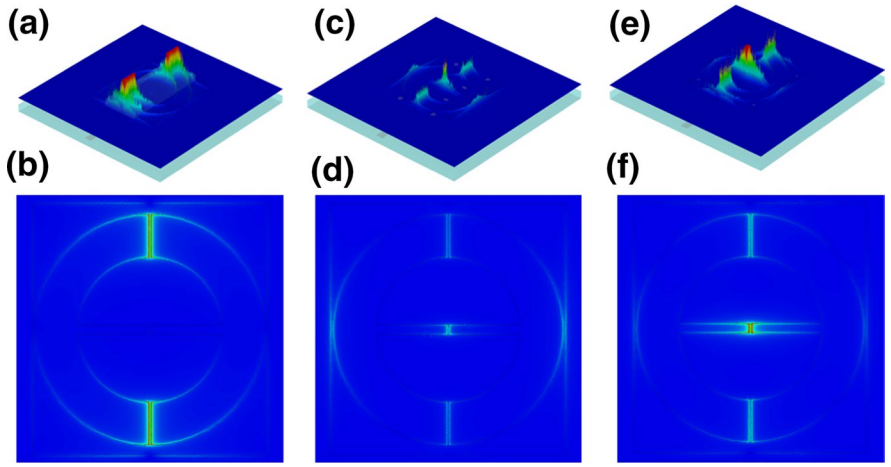

Fig. 3 Electromagnetic simulation of the spatial distributions of the magnetic component of Modes #1 (**a**, **b**), #2 (c,d) and #3 (e,f) of IAR A1. The 3D plots on top show the magnitude of the MW field taken at the surface of the resonator. Each plot on bottom shows a zoom of the top view of each distributions. For each mode, colorscale is normalized as described in Sect. 5.3, with red color being the maximum and blue color being zero

field intensity is reached in the central one. The comparison between Modes #2 and #3 shows that the largest confinement of the MW field in the central region (i.e., without appreciable currents circulating in the outer part of the device) is achieved for Mode #3.

2.3 Continuous-Wave Transmission Spectroscopy with IARs

We characterize the magnetic coupling of our IARs with a sample of α,γ-bisdiphenylene-β-phenylally (BDPA, for short) diluted in a polystyrene matrix, with a nominal density of $\approx 1 \cdot 10^{15}$ spin/mm^3. The $\approx 4.5 \times 2 \times 0.43$ mm^3 sample is placed on top of the resonator in order to cover the central part of the device, in particular the three conducting strips, as in Fig. 1. No significant changes in the Q-factor or in the resonant frequency are found on Modes #1, #2, #3 when the sample is added. The static magnetic field is applied parallel to the longitudinal axis of the transmission line. The sample is cooled at low temperature and the CW transmission spectra are acquired as a function of the static magnetic field with a Vector Network Analyzer (VNA, see Sect. 5 for details).

We report in Fig. 4 the CW transmission spectra obtained for Mode #1 and #3. For each resonant frequency, the shift of the resonant frequency and its corresponding normalized intensity as a function of the externally applied static magnetic field are given. The transmission intensity is normalized to the level given by the depth of each corresponding zero field transmission dip, to allow for comparison with the coplanar geometries. A shift of the resonant frequency and a corresponding increase of the transmission level is found around each resonant field value for all modes. This behavior shows that the sample is in the weak coupling regime [11, 39].

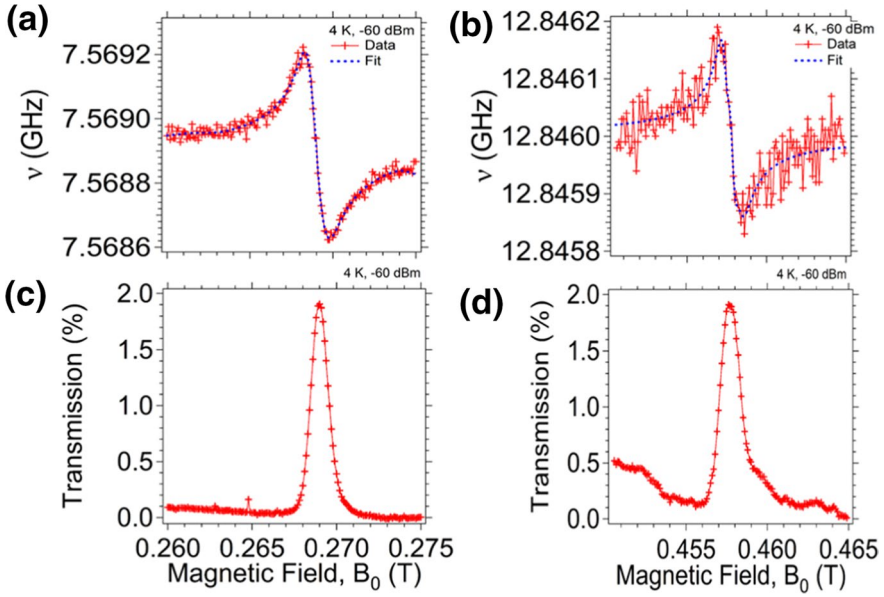

Fig. 4 CW transmission spectroscopy of BDPA organic radical coupled to IAR A1 for Mode #1 (7.56 GHz, **a**–**c**) and for Mode #3 (12.84 GHz, **b**–**d**). Frequency shift of the resonator (**a**–**b**) and corresponding signal intensity (**c**–**d**) as a function of the static magnetic field are shown. Black dashed lines are fits based on Eq. 1. All measures are taken at 4 K and −60 dBm (color figure online)

$$\nu = \nu_0 + \sum_{j}^{\#lines} \frac{\Omega_j^2(\nu_0 - \nu_{S,j})}{(\nu_0 - \nu_{S,j})^2 + \gamma_j^2} \tag{1}$$

We fit the frequency shift as a function of the static magnetic field with Eq. 1 (dashed lines of Fig. 4), which is based on the analogy between the coupled resonator and ensemble and an equivalent lumped element electrical network [11, 23]. For each jth line, $\Omega_j = \Omega_{S,j}\sqrt{N_{\mathrm{eff},j}}$ is its corresponding collective coupling rate, which depends on the single spin coupling rate, $\Omega_{S,j}$, and the effective number of spins involved, $N_{\mathrm{eff},j}$. The parameter γ_j is the half-width-half-maximum of each line, while $\nu_{S,j} = g_j\mu_B B_0/h$ is the Zeeman frequency, which depends on the Landè g-factor, g_j. For each line, we treat $\Omega_{S,j}, \gamma_j,$ and g_j as free parameters for fittings. We find that at least 5 lines are needed in order to properly reproduce the measured frequency shift, with two of them giving the main central signal. This is consistent with what was previously observed also in Ref. [22, 40, 41] for ESR spectroscopy of similar samples of BDPA diluted in polystyrene.

We report in Fig. 5 the coupling rate and the linewidth obtained from the data of Fig. 4 as a function of the frequency of each mode. The linewidth measured by IAR is slightly larger than the corresponding one measured by the Reference coplanar resonator. We attribute this effect to the less homogeneous MW field of IAR geometry. The coupling rates are on the order of 1–2 MHz, while the linewidth is always around 8-10 MHz, confirming that BDPA is weakly coupled to the resonator.

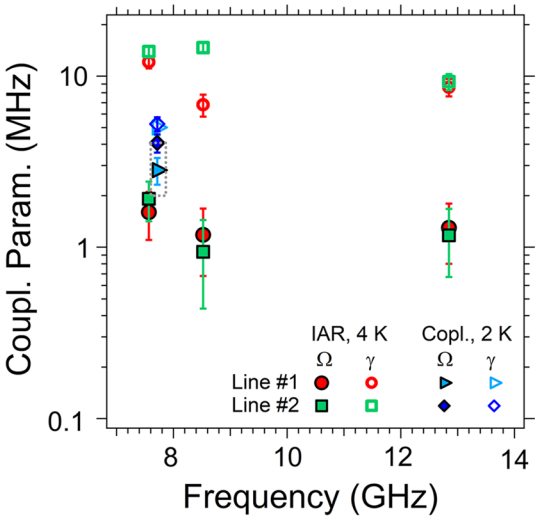

Fig. 5 Coupling parameters extracted for each of the three modes of IAR A1 at 4 K using the spectra of BDPA shown in Fig. 2. Points obtained for the same sample coupled to the reference coplanar resonator at 2 K (light blue and blue symbols) are added for comparison. Dashed rectangle shows the range of values of the coupling rate of lines #1 and #2 of BDPA with the Reference resonator between 2 and 5 K (see Supplementary Information) (color figure online)

Although a direct comparison between the collective coupling rates is difficult, we can argue that the coupling values found for IAR (at 4 K) are smaller than the ones found for the coplanar resonator between 2 and 5 K, with only the values found for these latter temperature being very close to the ones of IAR (see dashed rectangle in Fig. 5). Since we have larger single spin coupling rates for IAR geometries, this necessarily implies that the effective number of spins involved in the coupling is smaller.

2.4 Pulsed-Wave Transmission Spectroscopy with IARs

We now consider the PW regime of MW excitation. We use the same IAR and sample described above under the same experimental conditions and configuration of Fig. 1. The setup used for the generation of the pulses and for time-domain signal acquisition has been previously developed and described in [38], in which an additional output amplifier has been added (see Sect. 5.4 for further details). Since all three modes of IAR are found to respond to single-pulse MW excitations (see Supplementary Information), it turns out that it is possible to address BDPA spin ensemble and to manipulate it through the IAR. After preliminary tests and pulse calibrations, BDPA is found to give a Hahn echo when resonantly coupled to Modes #1, #2 and #3 (see Supplementary Information). The comparison of the echo signal obtained from the same BDPA sample on the large coplanar resonator previously used in [38] (see Fig. 6 and Supplementary Information) shows that the echo signal is rather small, as expected from the much lower number of spins involved in the coupling and addressed by the pulses. In particular, since the echo signal measured for Mode #2 is found to be the weakest among the three IAR modes and its intensity is comparable with background, we restrict our investigations only to Mode #1 and #3. Further analysis and checks of the echo signal shows that the MW pulses cannot individually address line #1 and #2, and that the echo signal visible is arising from their joint dynamics. The detection of a Hahn echo

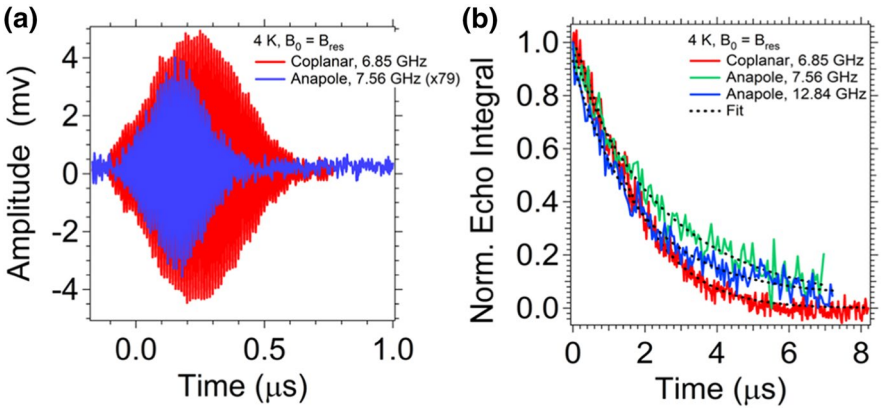

Fig. 6 Pulsed-wave transmission spectroscopy of BDPA on IAR A1. **a** Comparison between the Hahn echo signal obtained with the BDPA sample on a large coplanar resonator (red trace) at ≈ 6.91 GHz and IAR A1 excited on Mode #1 (blue trace), respectively. The signals were obtained using a different output amplification gain (see legend and Sec. 5.5). **b** Decay of the normalized integral of the Hahn echo measured for the large coplanar resonator (red) and for Mode #1 (7.56 GHz, green trace) and Mode #3 (12.84 GHz, blue trace) of IAR A1 at 4 K. Note that different pulses durations and powers are used for each measurement. Dashed lines are fits based on Eq. 2 (color figure online)

by the IAR demonstrates the possibility of coherently manipulating BDPA using this resonator.

Figure 6 shows the integral of each echo signal obtained from Modes #1 and #3 as a function of twice the delay between the $\pi/2$ and the π pulses. Each trace is normalized over its maximum value (which is the one found for $t_0 = 0$) according to the procedure previously used in [38]. The decay measured for the large coplanar resonator is added for comparison. The echo signals are found to decay over the same timescale giving comparable memory time, despite the different resonators and frequencies used. A slight increase in the decay time is observed for IAR with respect to the coplanar resonator. However, here we note that the large noise level does not allow us to analyze this effect in more details.

$$A(t - t_0) = A(t_0)e^{-(\frac{t-t_0}{T_m})^x} \tag{2}$$

We fit the data of Fig. 6 with the stretched exponential decay of Eq. 2. Here t_0 is the initial time, while $A(t_0)$ is its corresponding amplitude. T_m is the phase memory time, while x is a phenomenological stretch parameter and is treated as fit parameters. The

Table 1 Memory time and exponent obtained for IAR A1 and reference coplanar resonator (see Fig. 6) by means of Eq. 2

Resonator	T_m (μs)	x
Coplanar	1.8 ± 0.1	1.2 ± 0.1
IAR, Mode#1	2.3 ± 0.2	0.9 ± 0.3
IAR, Mode#3	1.9 ± 0.3	0.9 ± 0.3

results are summarized in Table 1. The memory time is around 2 µs for all the investigated resonators and modes, and it is also consistent with the values reported in the literature [16]. The stretch exponent found for coplanar resonator is in agreement with the one previously reported in [38] for a similar resonator. We ascribe the slight reduction of the stretch exponent to the different MW field distribution over the sample volume in the IAR comparing with the coplanar resonator.

We finally mention that we tested Rabi oscillations on BDPA both with both IAR and reference coplanar resonator, and the results are reported in Supplementary Information.

3 Discussion

3.1 Number of Spins in CW

We estimated the effective number of spins thanks to $\Omega = \Omega_S\sqrt{N_{\text{eff}}} = \Omega_S\sqrt{N_0 P(T)}$ [11, 42]. Here, N_0 is the zero temperature limit for the effective number of spins, which also corresponds to the maximum number of spins the resonant mode can couple, while $P(T)$ is the spin polarization as a function of temperature. We use a Curie–Weiss law in the form $P(T) = 1/(T - T_C)$ to model the spin polarization, being $T_C = -1$ K the Curie temperature (see Supplementary Information for details). The single spin coupling rate of each resonant mode has been independently estimated and is $\Omega_S = 6.4, 3$ and 8.9 Hz for the Mode #1, #2 and #3, respectively. We use the equation above to estimate N_{eff} and then N_0 (provided $T = 4$K). The total number of spins involved results to be on the order of $N_0 \approx 10^{11}$-10^{12} for both lines #1 and #2 and for all three resonant modes. Since the spin density of the sample is known, this allows us to estimate corresponding effective volumes on the order or $V_{eff} = 3 \cdot 10^4$-$5 \cdot 10^5\ \mu m^3$, which corresponds to tens up to few hundreds of picoliters. These values are approximately 2–3 orders of magnitude smaller than those found on measurements of the same sample with coplanar resonator ($N_0 \approx 1 \cdot 10^{14}$, see Supplementary Information). These effective mode volume estimations are also corroborated by additional electromagnetic simulations (see Supplementary Information).

3.2 Spin Sensitivity

We estimate the CW spin sensitivity for both lines #1 and #2 according to Eq. 3 and the method previously used in [37]. Briefly, the minimum number of spins N_{min} is estimated through Eq. 1, by searching the coupling rate value minimizing the frequency shift of each line down to its minimum value detectable over the noise level (the fitted linewidth value is used). The corresponding *signal-to-noise* ratio (SNR), $\frac{S}{N}|_{\text{min}}$, is then evaluated and used for calculation (the noise level is measured as the root-mean-square of baseline fluctuation far from resonance). The bandwidth, *BW*, is given by the inverse of the acquisition time of the VNA. Here we note the sensitivity as in Eq. 3 can be further normalized to the signal linewidth (in magnetic

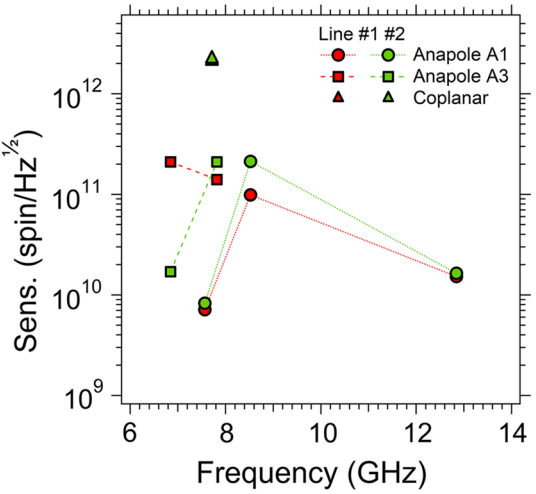

Fig. 7 CW spin sensitivity estimated according to Eq. 3 for IAR A1. Points obtained for previously reported coplanar resonators (Refs. [14, 37]) and IAR A3 coupled to same BDPA organic radical are added for comparison

field or frequency units), e.g., by dividing it with the full width at half maximum (FWHM, $\gamma_{\mathrm{FWHM},j} = 2\gamma_j$, according to our notations), giving Eq. 4 [17, 22, 26].

$$S = \frac{N_{\min}}{\frac{S}{N}|_{\min}\sqrt{BW}} \tag{3}$$

$$S' = \frac{N_{\min}}{\frac{S}{N}|_{\min}\sqrt{BW2\gamma}} \tag{4}$$

In Fig. 7 we report the sensitivity as a function of the resonant frequencies for Modes #1, #2 and #3. For comparison, we added points for our reference linear coplanar resonator and for the other Inverse Anapole Resonator (IAR A3, see Supplementary Information). The values found for our reference resonator are $S \approx 10^{12}\ \mathrm{spin}/\sqrt{Hz}$, in line with the values previously reported for the same resonator coupled to a Nitroxide organic radical crystal [37]. Anapole resonators show an improvement in the spin sensitivity of at least one order of magnitude (IAR A3) and reaching up to more than two orders of magnitude for Mode #1 and #3 of IAR A1, where $S = 8 \cdot 10^9\ \mathrm{spin}/\sqrt{\mathrm{Hz}}$. Similar improvement is found also looking at the normalized spin sensitivity S' (Eq. 4 and Supplementary Information).

To get more insights on our results, we compare our CW sensitivity with the values reported in the literature concerning planar microwave resonant geometries developed to couple to small samples. Results and the main features of each work are summarized in Table 2. We note that our values compare well with the ones reported in the previous

Table 2 Comparison between spin CW sensitivity and related experimental conditions for several planar microwave resonator developed for coupling to small spin ensemble volumes

Refs.	Resonator type	Material	Min. size (μm)	ν_0 (GHz)	T (K)	N	V_{eff} (nL)	S ($\frac{\text{spin}}{\sqrt{\text{Hz}}}$)	S' ($\frac{\text{spin}}{\sqrt{\text{HzmT}}}$)
[26]	IAR	Au	5	9.3	300	$5 \cdot 10^{10}$	0.05	–	$7 \cdot 10^{8}$
				9.8		$5 \cdot 10^{11}$			$4 \cdot 10^{9}$
[28]	Split ring	Cu	150	X band	300	–	$1 \cdot 10^{3}$	–	$3.7 \cdot 10^{12}$
[18]	Omega	Cu	20	14	2	$2 \cdot 10^{10}$	–	$^{1}D^{-1}$	–
					300	$1 \cdot 10^{11}$	–	$^{1}D^{-0.8}$	
[19]	Omega	Cu	200	13	300	–	0.5	$4.3 \cdot 10^{9}$	$2.3 \cdot 10^{10}$
				14			6.8	$3.2 \cdot 10^{10}$	$1.7 \cdot 10^{11}$
[23]	CMOS	Cu (?)	100	17	66	–	0.02	–	–
				20	300		0.4		
[4]	Microcoil	Cu	15	1.4	300	–	0.1	$2 \cdot 10^{10}$	$1 \cdot 10^{11}$
							0.2	$6 \cdot 10^{10}$	
[22]	CMOS	Al	45	49 90	30	$4 \cdot 10^{10}$	0.04	$2 \cdot 10^{7}$	$1 \cdot 10^{8}$
			120	140	300		0.2	$4 \cdot 10^{11}$	$8 \cdot 10^{8}$
[43]	CMOS	Cu/Al	80	27	77	$1 \cdot 10^{11}$	0.001	$2 \cdot 10^{8}$	$1 \cdot 10^{9}$
			100	27	300	$1 \cdot 10^{12}$	0.1		
[44]	CMOS	Al	100	9.4	300	–	0.1	$3 \cdot 10^{10}$	$1.5 \cdot 10^{11}$
				10					
This work	IAR A1	YBCO	50	7.5	2-5	$1.3 \cdot 10^{10}$	0.1	$8 \cdot 10^{9}$	$1 \cdot 10^{10}$
				12.8		$1.5 \cdot 10^{11}$	1		

Multiple values in some cell give the extremes of the working range used in each reference and do not necessary correspond to the values on same line. N is the number of spins reported in each work at the given temperature (this will be N_{eff} for our results). [1]Only scaling law normalized on 10^{10} spins is given, with D being the diameter of the inductor

work on IARs [26]. It is worth mentioning that in Ref. [26] the width of the central conductor is 5 µm instead of 50 µm used in our work. Overall, our results compare well also with other resonators based on either different geometries (e.g., Ω resonators) or technologies (e.g., CMOS oscillators), if one also takes into account also the various operating frequencies of resonators given in the literature. The effective number of spins and the corresponding effective volume is consistent with the values reported in the literature, corroborating the possibility of probing samples with sub-nanoliter volumes.

We now extend the analysis and the comparison above to the PW regime. In this case a spin sensitivity, S, and its corresponding normalized one, S', can be defined by means of Eqs. 5 and 6, respectively [17, 33].

$$S = \frac{N_{\text{echo}}}{\frac{S}{N}\sqrt{\text{BW}}} \tag{5}$$

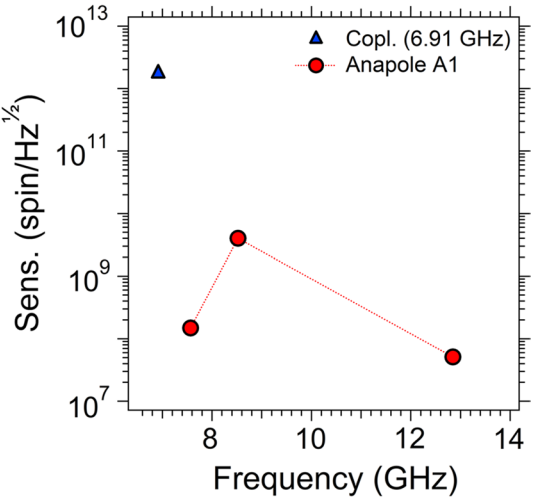

Fig. 8 Spin sensitivity estimated according to Eq. 3 for Inverse Anapole Resonator A1. Point obtained for previously reported coplanar resonator [38] coupled to the same BDPA organic radical is added for comparison

$$S' = \frac{N_{\text{echo}}}{\frac{S}{N}\sqrt{\text{BW}2\gamma}} \tag{6}$$

These equations are formally identical to the ones used in CW, but the quantities now have a different physical meaning. Here N_{echo} is the number of spins taking part to the measured echo signal (it is implicitly assumed that a spin echo must be used to estimate the sensitivity and, consequently, that a pulse sequence at least equal to Hahn's one must be applied to the spins). The signal-to-noise ratio $\frac{S}{N}$ is measured on the output echo signal. Here we note that there is a general consensus in using this quantity as it comes from the final measure, without considering the effect of averaging over different acquisitions (which, if done, would give a rescaling factor $(S/N)|_{\text{single shot}} = (S/N)/\sqrt{\#avr}$, with $\#avr$ the number of averages) [24, 33]. Conversely, there is a general agreement on the fact that using pulse sequences with larger number of π pulses with respect to Hahn's one (e.g., Carr–Purcell–Meiboom–Gill, CPMG) improves the signal-to-noise ratio as $(S/N)|_{\text{CPMG}} = (S/N)|_{\text{Hahn}}\sqrt{\#avr}$ [24, 33]. Finally, the bandwidth is given by the repetition rate of the sequence used.

Based on these considerations, we estimate spin sensitivity in the PW regime for all three modes of IAR and for our reference coplanar resonator. In particular since lines #1 and #2 of BDPA are contributing to the same echo signal (see Sect. 2.4), a unique value of sensitivity S (and then S') is given for each resonant frequency value. The number of spins contributing to the echo is evaluated according to the method described in the Supplementary Information. Our results are given in Fig. 8. It is clear that the sensitivity of IAR exceeds by up to more than 3 orders of magnitude

Table 3 Comparison between spin PW sensitivity and related experimental conditions for several planar microwave resonator developed for coupling to small spin ensemble volumes

Refs.	Resonator type	Material	Min. size (μm)	ν_0 (GHz)	T (K)	N_{eff}	Seq.	V_{eff} (nL)	S ($\frac{spin}{\sqrt{Hz}}$)
[20]	Loop gap	Au	50	12	300	–	Hahn	1	$1.8 \cdot 10^8$
	Omega			17				10	$4.5 \cdot 10^8$
[21]	Loop gap	Cu	2	10	300	–	Hahn	0.04	$6.4 \cdot 10^7$
			150	17	300	–	Hahn	6.9	$1.2 \cdot 10^9$
	Loop gap	Cu	2	10	10	–	Hahn	0.04	$2.9 \cdot 10^4$
			150	17				6.9	$3.6 \cdot 10^5$
[24]	ParPar	Cu	20	35	10	$5.7 \cdot 10^9$	CPMG 180 π	0.1	$6.9 \cdot 10^5$
				36	300				([1] $9.2 \cdot 10^6$)
		YBCO	50	35	10		CPMG 180 π	0.1	$5.8 \cdot 10^5$
				36	77				([1] $7.8 \cdot 10^6$)
[25]	ParPar	Cu	20	34	50	$2 \cdot 10^{11}$	Hahn	0.4	$1.3 \cdot 10^8$
				36	300			6.2	$2.3 \cdot 10^8$
						$2 \cdot 10^{11}$	CPMG 161 π	0.4	$6.3 \cdot 10^5$
								6.2	([1] $8 \cdot 10^6$)
[33]	Lumped element	Al	1	7	0.012	$1.2 \cdot 10^4$	Hahn	0.02	$1.3 \cdot 10^3$
						$1.3 \cdot 10^3$	CPMG 600 π	0.02	$1.5 \cdot 10^2$
[29]	Lumped element	Nb	2	4.96	0.02	$1.5 \cdot 10^5$	Hahn	-	$2 \cdot 10^4$
[35]	Lumped + nanowire	Al	0.5	7.27	0.012	$2 \cdot 10^2$	Hahn	$2 \cdot 10^{-4}$	65
						–	CPMG 200 π	–	33
[34]	Lumped	Al	0.1	7.2	0.02	36	Hahn	$6 \cdot 10^{-6}$	12
	+ nanowire			7.5					
						–	CPMG 20 π	–	6
This work	IAR	YBCO	50	7.5	2	$3.8 \cdot 10^{10}$	Hahn	0.1	$6 \cdot 10^7$
	A1			12.8	5	$2.4 \cdot 10^{11}$		0.2	$1 \cdot 10^8$

Multiple values in some cell give the extremes of the working range used in each reference and do not necessary correspond to the values on same line. Note that we do not give the sensitivity S' since its value is given in the literature. [1]Values are normalized to the square root of the number of π pulses to refer to a simple Hahn echo sequence, see [33]

that of reference coplanar resonator. The maximum sensitivity $S \approx 6 \cdot 10^7$ spin/$\sqrt{\text{Hz}}$ is achieved on Mode #3.

In Table 3 we compare our results with the values reported in the literature concerning planar microwave resonant geometries developed to couple to small samples and in which PW experiments are reported. Worth to notice that, to the best of our knowledge, this work is the first report of PW manipulation of a spin ensemble with IARs. Our sensitivity compares well with the values obtained using Hahn echo sequences and similar working frequencies (Ref. [20, 21]). The sensitivity can be improved by 2 or 3 orders of magnitude by using resonant geometries with larger resonant frequencies and using CPMG sequences instead of simple Hahn echo ones, as in Ref. [24, 25]. Here we also note that our echo signals were measured indirectly with the transmission line, after the weak currents induced by them into the IAR went through the relatively large thickness of the Sapphire substrate (430 μm). Using substrates with smaller thicknesses ($\approx 200\,\mu$m as in [24, 25]) would improve the coupling between IAR and transmission line and the possibility of picking-up larger signals (and improving the signal-to-noise ratio). Further improvement in the detection inductance of the resonator would further increase the sensitivity, as shown in [33–35].

4 Conclusion

In conclusion, we designed and fabricated Inverse Anapole Resonators made of superconducting YBCO/Sapphire films and working at microwave frequency, and we then tested them with BDPA organic radical diluted in a matrix of polystyrene. In the CW regime of excitation the system consisting of IAR and spin ensemble is found to be in the weak coupling regime for each resonant mode. Further analysis reveals that typical effective volumes involved in the coupling are on the order of 0.1 nL ($\approx 10^5\,\mu m^3$), and that spin sensitivities $S = 8 \cdot 10^9$ spin/$\sqrt{\text{Hz}}$ (or equivalently $S' = 1 \cdot 10^{10}$ spin/(mT $\sqrt{\text{Hz}}$)) can be achieved. The comparison with the sensitivity achieved with our linear coplanar resonator and the same sample shows an improvement of up to more than 3 orders of magnitude. Our sensitivities compare well with the values reported in the literature on similar planar resonant geometries. In the PW regime of excitation, the Hahn echo signal was observed for all the modes of IAR, demonstrating the possibility of manipulating sub-nanoliter volumes of BDPA spin ensembles coherently. Thus, our results are very promising in the view of the application of IARs in ESR or hybrid quantum systems, considering the large thickness of the Sapphire substrate which separates the IAR from the feed line. Moreover, it was also possible to measure the memory time of BDPA and to observe Rabi oscillations. The PW sequences performed on the same sample with a linear coplanar resonator reveal comparable memory time and a slightly slower decay of the Rabi oscillation, probably

due to the lower MW field inhomogeneity. Further analysis allowed us to estimate an effective number of coupled spins $N_{\mathrm{eff}} \approx 10^{10}$-$10^{11}$ (corresponding to $\approx$ 0.1-0.2nL) and a PW spin sensitivity $S \approx 10^{7}$-$10^{8}\,\mathrm{spin}/\sqrt{\mathrm{Hz}}$ (or, equivalently, $S' \approx 10^{7}$-$10^{8}\,\mathrm{spin}/(\mathrm{mT}\sqrt{\mathrm{Hz}})$). The comparison of the sensitivity with our previous results on coplanar linear resonator shows an improvement in more than 3 orders of magnitude. The comparison with the literature reveals that, although the performances of our IARs are in line with some reports, further improvements can be done. In particular, the sensitivity would benefit from further modifications in the geometry (e.g., shrinking the size of the central conductor, reducing the thickness of the substrate) as well as in improving the output amplification (e.g., adding a low-noise cryogenic amplifier in proximity of the device).

5 Methods

5.1 BDPA Organic Radical sample

Our α,γ-bisdiphenylene-β-phenylally (BDPA) organic radical was diluted into a polystyrene matrix, reaching a nominal spin density of $\approx 1 \cdot 10^{15}$ spin/mm^3. Our sample was prepared by first dissolving polystyrene in toluene and then adding commercial concentrated BDPA powder (0.08 % by weigh BDPA to polystyrene). Toluene is then let evaporate to obtain a film sample, which was then cut into a parallelepiped shape with dimensions $\approx 4.5 \times 2 \times 0.43\,\mathrm{mm}^3$. For comparison we mention that a pure 100% BDPA powder (with no polystyrene) has a concentration of $\approx 1.5 \cdot 10^{18}$ spin/mm^3 [16]. Additional information on BDPA is given in Supplementary Information.

5.2 Fabrication of the Resonators

Our resonators were designed and adapted starting from the geometry previously reported in [26]. We fabricate the resonators from 5×8 mm^2 single-sided YBCO/Sapphire commercial films purchased from Ceraco company. The resonators are patterned by optical lithography with positive photoresist followed by etching with argon plasma in a reactive ion etching (RIE) chamber to remove the excess YBCO. The YBCO transmission line is fabricated from commercial 10×10 mm^2 double-sided YBCO/Sapphire films by optical lithography followed by wet chemical etching, according to the procedure previously reported in [14]. The bottom YBCO film is used as ground plane for the transmission line.

The linear coplanar resonators used as reference for CW and PW spectroscopy are the ones previously investigated in [14] and in [12, 38], respectively. Both resonators were fabricated by optical lithography follower by wet chemical etching starting from commercial 10×10 mm^2 double-sided YBCO/Sapphire films.

5.3 Electromagnetic Simulations

Electromagnetic simulations of the whole devices (IAR and its transmission line) have been carried out with the CST Microwave software. A 1:1 scale model of the device has been designed and then simulated in order to extract the MW field distributions. The superconducting YBCO parts were treated as Perfect Electric Conductor (PEC), while $\epsilon_r = 10.77$ and $\tan\delta = 1 \cdot 10^{-6}$ have been used for the Sapphire substrate. The input power given to the ports of the model during simulation was fixed to 1 W. For the field distributions shown in this work, the magnitude of the MW field has been normalized over the same maximum value of 30 mT for better comparison.

To estimate the effective mode volume, a 1:1 scale model of the sample was added on top of the resonator. The effective mode volume was estimated by calculating the integral of the squared of the (normalized) MW field distribution over the sample volume, in a similar way to the method previously used also in [12]. To take into account the finite extension of the MW distribution, a cutoff value was used during integration (see Supplementary Information).

5.4 CW Transmission Spectroscopy

The transmission line was mounted in an Oxygen-Free High Thermal Conductivity shielding box equipped with SMA connectors and launching antennas, as previously described in [11, 14]. The edges of the line are glued to the antennas with silver epoxy paint in order to provide electrical contact with the MW lines and the external MW electronics. The resonator was then placed on top of the transmission line and glued with a small amount of vacuum grease, and it was carefully aligned to its final position (see Fig. 1) under optical microscope. Finally, the sample is placed on top of the IAR and glued with a small amount of silicone vacuum grease.

Continuous-wave transmission spectroscopy was carried out with the same setup previously reported in [11]. Briefly, the resonator box is mounted on a low-temperature probe equipped with MW coaxial line and thermometer and inserted in a Quantum Design Physical Property Measurements System (QD PPMS), which is used to cool down the sample and to apply the static magnetic field. The transmission spectra of the device are measured with a Vector Network Analyzer (VNA). Additional room temperature attenuators and amplifiers are added on the input and on the output line, respectively. A total attenuation of 60 dB (MW line + attenuators) and total output gain of 74 dB are achieved in this configuration. In this paper, if not otherwise specified, all the power values given will refer to the level of the input antenna inside the shielding box. Neglecting the attenuation given by half of the microstrip transmission line ($\approx$ 5mm) with respect to the total length of the input MW line ($\approx$ 1.5m), this will correspond approximately to the input power available on the back side of IAR.

5.5 PW Transmission Spectroscopy

Pulsed-wave transmission spectroscopy on the reference coplanar resonator was carried out with the previously developed setup reported in [38]. It is a home-made heterodyne spectrometer based on an Arbitrary Waveform Generator (AT ARB Rider AWG-4022 by Active Technologies) with tunable probing frequency. Due to the small signals expected, the setup was modified for working with IARs. In particular, the input amplifier was replaced by a power amplifier (Mini-Circuits ZVE-3W-183+, 35 dB gain), while two voltage amplifiers (Fairview Microwave SLNA-180-38-25-SMA, 38 dB gain each) were used on the output line before the detection mixer.

For each different resonator and working frequency the MW pulses were first calibrated within a two-pulses calibration procedure in order to maximize the amplitude of the echo signal given by BDPA. A relaxation time of 30 ms was added at the end of each sequence to avoid sample saturation. This time gives the sequence repetition rate and the detection BW used in estimating the PW sensitivity [24, 33].

For the reference coplanar resonator the Hahn echo experiment was carried out using MW pulses with duration of 150 and 300 ns for the $\pi/2$ and π rotation, respectively. The initial interpulse delay was set to $\tau = 900$ ns, and 2000 averages for each point of echo decay step were taken. The MW attenuation level used before the input power amplifier was set to zero decibel. The pulse parameters for each mode of IAR were found to be quite different. Hahn echo sequence was found to give an optimal echo on Mode #1 using $t_{\pi/2} = 100$ns and $t_{\pi} = 200$ns, an initial interpulse delay $\tau = 500$ ns with attenuation of 0 dB, while the best parameters obtained for Mode #3 were $t_{\pi/2} = 300$ns and $t_{\pi} = 700$ns, an initial interpulse delay $\tau = 400$ ns with attenuation of 0 dB. For both modes the number of averages of the echo decay point was set to 2000.

Supplementary Information The online version contains supplementary material available at https://doi.org/10.1007/s00723-022-01505-8.

Acknowledgements We thank Dr. Dorsa Komijani (previously at National High Magnetic Field Laboratory, Tallahassee, Florida, USA) for additional discussion on BDPA sample. This work was funded by the H2020-FETOPEN "Supergalax" project (Grant Agreement No. 863313) supported by the European Community and supported by NATO Science for Peace and Security Programme (NATO SPS Project No. G5859). MM acknowledges TUBITAK-BIDEB for the 2219 scholarship program. The National High Magnetic Field Laboratory is supported by the National Science Foundation through NSF/DMR-1644779 and the State of Florida.

Author Contributions Data on CW transmission spectroscopy were collected by CB and MM. Data on PW transmission spectroscopy were collected by CB. All data analysis has been carried out by CB. MM carried out the electromagnetic simulations of the resonators. IARs were fabricated by AG and MM. The BDPA sample was prepared by JvT. The paper was written by CB with inputs from all authors. MA, BR, AG, MM, CB conceived the experiment. The manuscript has been revised by all authors before submission.

Availability of Data and Materials The data that support the findings of this study are available from the corresponding author upon reasonable request.

Declarations

Conflict of Interest The authors declare no competing or financial interests.

Editorial Policies for: Springer journals and proceedings: https://www.springer.com/gp/editorial-policies

References

1. J.J.L. Morton, P. Bertet, Storing quantum information in spins and high-sensitivity esr. J. Magn. Reson. **287**, 128–139 (2018). https://doi.org/10.1016/j.jmr.2017.11.015
2. A.A. Clerk, K.W. Lehnert, P. Bertet, J.R. Petta, Y. Nakamura, Hybrid quantum systems with circuit quantum electrodynamics. Nat. Phys. **16**(3), 257–267 (2020)
3. A. Imamoğlu, Cavity qed based on collective magnetic dipole coupling: spin ensembles as hybrid two-level systems. Phys. Rev. Lett. **102**, 083602 (2009). https://doi.org/10.1103/PhysRevLett.102.083602
4. G. Boero, M. Bouterfas, C. Massin, F. Vincent, P.-A. Besse, R.S. Popovic, A. Schweiger, Electron-spin resonance probe based on a 100 μm planar microcoil. Rev. Sci. Instrum. **74**(11), 4794–4798 (2003). https://doi.org/10.1063/1.1621064
5. D.I. Schuster, A.P. Sears, E. Ginossar, L. DiCarlo, L. Frunzio, J.J.L. Morton, H. Wu, G.A.D. Briggs, B.B. Buckley, D.D. Awschalom, R.J. Schoelkopf, High-cooperativity coupling of electron-spin ensembles to superconducting cavities. Phys. Rev. Lett. **105**, 140501 (2010). https://doi.org/10.1103/PhysRevLett.105.140501
6. Y. Kubo, F.R. Ong, P. Bertet, D. Vion, V. Jacques, D. Zheng, A. Dréau, J.-F. Roch, A. Auffeves, F. Jelezko, J. Wrachtrup, M.F. Barthe, P. Bergonzo, D. Esteve, Strong coupling of a spin ensemble to a superconducting resonator. Phys. Rev. Lett. **105**, 140502 (2010). https://doi.org/10.1103/PhysRevLett.105.140502
7. R. Amsüss, C. Koller, T. Nöbauer, S. Putz, S. Rotter, K. Sandner, S. Schneider, M. Schramböck, G. Steinhauser, H. Ritsch, J. Schmiedmayer, J. Majer, Cavity qed with magnetically coupled collective spin states. Phys. Rev. Lett. **107**, 060502 (2011). https://doi.org/10.1103/PhysRevLett.107.060502
8. S. Probst, H. Rotzinger, A.V. Ustinov, P.A. Bushev, Microwave multimode memory with an erbium spin ensemble. Phys. Rev. B **92**, 014421 (2015). https://doi.org/10.1103/PhysRevB.92.014421
9. C.W. Zollitsch, K. Mueller, D.P. Franke, S.T.B. Goennenwein, M.S. Brandt, R. Gross, H. Huebl, High cooperativity coupling between a phosphorus donor spin ensemble and a superconducting microwave resonator. Appl. Phys. Lett. **107**(14), 142105 (2015). https://doi.org/10.1063/1.4932658
10. J. O'Sullivan, O.W. Kennedy, C.W. Zollitsch, M. Šim ėnas, C.N. Thomas, L.V. Abdurakhimov, S. Withington, J.J.L. Morton, Spin-resonance linewidths of bismuth donors in silicon coupled to planar microresonators. Phys. Rev. Appl. **14**, 064050 (2020). https://doi.org/10.1103/PhysRevApplied.14.064050
11. C. Bonizzoni, A. Ghirri, M. Affronte, Coherent coupling of molecular spins with microwave photons in planar superconducting resonators. Adv. Phys. X **3**(1), 1435305 (2018)
12. C. Bonizzoni, A. Ghirri, M. Atzori, L. Sorace, R. Sessoli, M. Affronte, Coherent coupling between vanadyl phthalocyanine spin ensemble and microwave photons: towards integration of molecular spin qubits into quantum circuits. Sci. Rep. **7**(1), 13096 (2017)
13. A. Ghirri, C. Bonizzoni, F. Troiani, N. Buccheri, L. Beverina, A. Cassinese, M. Affronte, Coherently coupling distinct spin ensembles through a high-T_c superconducting resonator. Phys. Rev. A **93**, 063855 (2016). https://doi.org/10.1103/PhysRevA.93.063855
14. A. Ghirri, C. Bonizzoni, D. Gerace, S. Sanna, A. Cassinese, M. Affronte, YBa_2 Cu_3 O_7 microwave resonators for strong collective coupling with spin ensembles. Appl. Phys. Lett. **106**(18), 184101 (2015). https://doi.org/10.1063/1.4920930

15. M. Mergenthaler, J. Liu, J.J. Le Roy, N. Ares, A.L. Thompson, L. Bogani, F. Luis, S.J. Blundell, T. Lancaster, A. Ardavan, G.A.D. Briggs, P.J. Leek, E.A. Laird, Strong coupling of microwave photons to antiferromagnetic fluctuations in an organic magnet. Phys. Rev. Lett. **119**, 147701 (2017). https://doi.org/10.1103/PhysRevLett.119.147701
16. S. Lenz, D. Kónig, D. Hunger, J. van Slageren, Room-temperature quantum memories based on molecular electron spin ensembles. Adv. Materi. https://doi.org/10.1002/adma.202101673
17. A. Blank, Y. Twig, Y. Ishay, Recent trends in high spin sensitivity magnetic resonance. J. Magn. Reson. **280**, 20–29 (2017). https://doi.org/10.1016/j.jmr.2017.02.019. (**Special Issue on Methodological advances in EPR spectroscopy and imaging**)
18. R. Narkowicz, D. Suter, I. Niemeyer, Scaling of sensitivity and efficiency in planar microresonators for electron spin resonance. Rev. Sci. Instrum. **79**(8), 084702 (2008). https://doi.org/10.1063/1.2964926
19. R. Narkowicz, D. Suter, R. Stonies, Planar microresonators for epr experiments. J. Magn. Reson. **175**(2), 275–284 (2005). https://doi.org/10.1016/j.jmr.2005.04.014
20. Y. Twig, E. Suhovoy, A. Blank, Sensitive surface loop-gap microresonators for electron spin resonance. Rev. Sci. Instrum. **81**, 104703 (2010). https://doi.org/10.1063/1.3488365
21. Y. Twig, E. Dikarov, A. Blank, Ultra miniature resonators for electron spin resonance: sensitivity analysis, design and construction methods, and potential applications. Mol. Phys. **111**(18–19), 2674–2682 (2013). https://doi.org/10.1080/00268976.2012.762463
22. A.V. Matheoud, G. Gualco, M. Jeong, I. Zivkovic, J. Brugger, H.M. Rønnow, J. Anders, G. Boero, Single-chip electron spin resonance detectors operating at 50 ghz, 92 ghz, and 146 ghz. J. Magn. Reson. **278**, 113–121 (2017). https://doi.org/10.1016/j.jmr.2017.03.013
23. G. Boero, G. Gualco, R. Lisowski, J. Anders, D. Suter, J. Brugger, Room temperature strong coupling between a microwave oscillator and an ensemble of electron spins. J. Magn. Reson. **231**, 133–140 (2013). https://doi.org/10.1016/j.jmr.2013.04.004
24. Y. Artzi, Y. Yishay, M. Fanciulli, M. Jbara, A. Blank, Superconducting micro-resonators for electron spin resonance—the good, the bad, and the future. J. Magn. Reson. **334**, 107102 (2022). https://doi.org/10.1016/j.jmr.2021.107102
25. N. Dayan, Y. Ishay, Y. Artzi, D. Cristea, E. Reijerse, P. Kuppusamy, A. Blank, Advanced surface resonators for electron spin resonance of single microcrystals. Rev. Sci. Instrum. **89**(12), 124707 (2018). https://doi.org/10.1063/1.5063367
26. N. Abhyankar, A. Agrawal, P. Shrestha, R. Maier, R.D. McMichael, J. Campbell, V. Szalai, Scalable microresonators for room-temperature detection of electron spin resonance from dilute, sub-nanoliter volume solids. Sci. Adv. **6**(44) (2020). https://doi.org/10.1126/sciadv.abb0620. https://advances.sciencemag.org/content/6/44/eabb0620.full.pdf
27. M.D. Jenkins, U. Naether, M. Ciria, J. Sesé, J. Atkinson, C. Sánchez-Azqueta, E.D. Barco, J. Majer, D. Zueco, F. Luis, Nanoscale constrictions in superconducting coplanar waveguide resonators. Appl. Phys. Lett. **105**, 162601 (2014). https://doi.org/10.1063/1.4899141
28. S.Z. Kiss, A.M. Rostas, L. Heidinger, N. Spengler, M.V. Meissner, N. MacKinnon, E. Schleicher, S. Weber, J.G. Korvink, A microwave resonator integrated on a polymer microfluidic chip. J. Magn. Reson. **270**, 169–175 (2016). https://doi.org/10.1016/j.jmr.2016.07.008
29. C. Eichler, A.J. Sigillito, S.A. Lyon, J.R. Petta, Electron spin resonance at the level of 10^4 spins using low impedance superconducting resonators. Phys. Rev. Lett. **118**, 037701 (2017). https://doi.org/10.1103/PhysRevLett.118.037701
30. N. Samkharadze, A. Bruno, P. Scarlino, G. Zheng, D.P. DiVincenzo, L. DiCarlo, L.M.K. Vandersypen, High-kinetic-inductance superconducting nanowire resonators for circuit qed in a magnetic field. Phys. Rev. Appl. **5**, 044004 (2016). https://doi.org/10.1103/PhysRevApplied.5.044004
31. N. Maleeva, L. Grünhaupt, T. Klein, F. Levy-Bertrand, O. Dupre, M. Calvo, F. Valenti, P. Winkel, F. Friedrich, W. Wernsdorfer, A.V. Ustinov, H. Rotzinger, A. Monfardini, M.V. Fistul, I.M. Pop, Circuit quantum electrodynamics of granular aluminum resonators. Nat. Commun. **9**(1), 3889 (2018)
32. P. Winkel, K. Borisov, L. Grünhaupt, D. Rieger, M. Spiecker, F. Valenti, A.V. Ustinov, W. Wernsdorfer, I.M. Pop, Implementation of a transmon qubit using superconducting granular aluminum. Phys. Rev. X **10**, 031032 (2020). https://doi.org/10.1103/PhysRevX.10.031032

33. A.J.P. Bienfait, Y. Kubo, M. Stern, X.C.L.D.W. Zhou, T.W.T.L. Schenkel, D. Vion, D. Esteve, B. Julsgaard, K.L.M.J. Mølmer, P. Bertet, Reaching the quantum limit of sensitivity in electron spin resonance. Nat. Nano **11**(3), 253–257 (2016)
34. V. Ranjan, S. Probst, B. Albanese, T. Schenkel, D. Vion, D. Esteve, J.J.L. Morton, P. Bertet, Electron spin resonance spectroscopy with femtoliter detection volume. Appl. Phys. Lett. **116**(18), 184002 (2020). https://doi.org/10.1063/5.0004322
35. S. Probst, A. Bienfait, P. Campagne-Ibarcq, J.J. Pla, B. Albanese, J.F. Da Silva Barbosa, T. Schenkel, D. Vion, D. Esteve, K. Molmer, J.J.L. Morton, R. Heeres, P. Bertet, Inductive-detection electron-spin resonance spectroscopy with 65 spins/ hz sensitivity. Appl. Phys. Lett. **111**(20), 202604 (2017). https://doi.org/10.1063/1.5002540
36. C. Bonizzoni, F. Troiani, A. Ghirri, M. Affronte, Microwave dual-mode resonators for coherent spin-photon coupling. J. Appl. Phys. **124**(19), 194501 (2018). https://doi.org/10.1063/1.5050869
37. C. Bonizzoni, A. Ghirri, S. Nakazawa, S. Nishida, K. Sato, T. Takui, M. Affronte, Transmission spectroscopy of molecular spin ensembles in the dispersive regime. Adv. Quant. Tech. **4**(9), 2100039 (2021). https://doi.org/10.1002/qute.202100039
38. C. Bonizzoni, A. Ghirri, F. Santanni, M. Atzori, L. Sorace, R. Sessoli, M. Affronte, Storage and retrieval of microwave pulses with molecular spin ensembles. NPJ Quant. Inform. **6**(1), 68 (2020)
39. C. Bonizzoni, A. Ghirri, K. Bader, J. van Slageren, M. Perfetti, L. Sorace, Y. Lan, O. Fuhr, M. Ruben, M. Affronte, Coupling molecular spin centers to microwave planar resonators: towards integration of molecular qubits in quantum circuits. Dalton Trans. **45**, 16596–16603 (2016). https://doi.org/10.1039/C6DT01953F
40. C. Caspers, P.F. da Silva, M. Soundararajan, M.A. Haider, J.-P. Ansermet, Field and frequency modulated sub-thz electron spin resonance spectrometer. APL Photon. **1**(2), 026101 (2016). https://doi.org/10.1063/1.4945450
41. S. Mitsudo, K. Kono, K. Dono, K. Hayashi, Y. Ishikawa, Y. Fujii, Ft-esr measurements on bdpa by pulsed esr using a gyrotron as high-power millimeter wave source. In: 2019 44th International Conference on Infrared, Millimeter, and Terahertz Waves (IRMMW-THz), pp. 1–1 (2019). https://doi.org/10.1109/IRMMW-THz.2019.8874493
42. M. Jenkins, T. Hümmer, M.J. Martínez-Pérez, J. García-Ripoll, D. Zueco, F. Luis, Coupling single-molecule magnets to quantum circuits. N. J. Phys. **15**, 095007 (2013)
43. J. Anders, A. Angerhofer, G. Boero, K-band single-chip electron spin resonance detector. J. Magn. Reson. **217**, 19–26 (2012). https://doi.org/10.1016/j.jmr.2012.02.003
44. T. Yalcin, G. Boero, Single-chip detector for electron spin resonance spectroscopy. Rev. Sci. Instrum. **79**(9), 094105 (2008). https://doi.org/10.1063/1.2969657

Authors and Affiliations

Claudio Bonizzoni[1,2] · Maksut Maksutoglu[3] · Alberto Ghirri[2] · Johan van Tol[4] · Bulat Rameev[3] · Marco Affronte[1]

Maksut Maksutoglu
mmaksutoglu@gtu.edu.tr

Alberto Ghirri
alberto.ghirri@nano.cnr.it

Johan van Tol
vantol@magnet.fsu.edu

Bulat Rameev
rameev@gtu.edu.tr

Marco Affronte
marco.affronte@unimore.it

[1] Dipartimento di Scienze Fisiche, Informatiche e Matematiche, Università di Modena e Reggio Emilia, Via G. Campi 213/A, 41125 Modena, Italy

[2] Istituto Nanoscienze-CNR, Via G. Campi 213/A, 41125 Modena, Italy

[3] Physics Department, Gebze Technical University, 41400 Gebze, Kocaeli, Turkey

[4] National High Magnetic Field Laboratory, Florida State University, Paul Dirac Drive 1800 E, Tallahassee, FL 32310, USA